Controlled parametric forcing during directional solidification of a bulk organic alloy under microgravity

F.L. Mota[a], K. Ji[b,c], Y. Song[b,c], L. Littles[d], A. Karma[b], N. Bergeon[a]*

[a] *Aix Marseille Univ, CNRS, IM2NP, Marseille, France*

[b] *Department of Physics for interdisciplinary research on Complex Systems, Northeastern University, Boston MA 02115, USA*

[c] *Materials Science Division, Lawrence Livermore National Laboratory, Livermore, CA 94550, USA*

[d] *Marshall Space Flight Center, Huntsville, USA*

* fatima.lisboa-mota@cnrs.fr

Keywords: directional solidification, alloy, transparent model systems, transient solidification, microgravity

Abstract

The response of dendritic microstructures to step-like pulling velocity conditions is investigated using microgravity directional solidification experiments conducted on DECLIC-DSI combined with phase-field simulations. Under a constant pulling velocity of 1.5 µm/s, the evolution toward steady-state growth is characterized in terms of primary spacing, dendrite drift, and tip dynamics. For the first time, side-view observations enabled direct measurement of tip radius and sidebranching frequency. When step-like oscillations of the pulling velocity are imposed, the dendritic array exhibits a strongly period-dependent response: short periods lead to rapid tip adaptation, whereas longer periods induce a phase lag between tip position and morphology, resulting in progressive tip flattening and, above a critical period, interface destabilization and dendrite splitting. Quantitative phase-field simulations, including a realistic thermal field and stochastic noise, reproduce the experimental observations and provide insight into the governing mechanisms, highlighting the role of characteristic relaxation times, sequence-dependent effects, and the irreversible reorganization of the microstructure following splitting.

Introduction

Solidification microstructures strongly influence the mechanical and physical properties of materials such as metallic alloys. The relationship between microstructure formation and processing conditions can

be investigated through directional solidification experiments, in which all the relevant parameters can be independently controlled.[1,2] Most theoretical models assume diffusive heat and mass transport and have been validated by comparisons with well-controlled experiments, many of which were performed in thin samples to suppress convection. In bulk samples, however, natural convection in the melt can disturb the homogeneity of the processing conditions and thus affect microstructure formation.[3-7] Experiments performed under microgravity conditions provide a unique opportunity to investigate interfacial pattern formation and microstructure development in spatially extended samples with negligible convection and well-controlled growth conditions.[8] Such experiments generate valuable benchmark data for testing theoretical and computational models under purely diffusive growth conditions.

The present study is based on experiments carried out with the Directional Solidification Insert (DSI), which was designed for *in situ* and real time characterization of the dynamical selection of solid-liquid interface morphologies in bulk samples of transparent materials. The DSI was developed by the French Space Agency (CNES) within the framework of the DECLIC project (DEvice for the study of Critical Liquids and Crystallization). The DECLIC facility was installed aboard the International Space Station (ISS) as part of a joint NASA/CNES research program. Two series of microgravity experiments were conducted aboard the ISS on samples of two different compositions. These experiments were monitored and controlled remotely in near real time.

Beyond providing insights into microstructure formation, the DECLIC-DSI experiments have generated a benchmark database for validating numerical simulations.[9,10] Analyses revealed the complex evolution of the thermal field in bulk samples and its influence on pattern selection,[11] motivating the development of phase-field simulations coupled with thermal calculations.[12] They also highlighted the role of interface curvature, sub-boundaries, and pattern misorientations inherent to three-dimensional growth.[13,14] In addition, unprecedented phenomena such as grain invasion mechanisms[15] and breathing-mode oscillations in extended cellular arrays[16-20] have been observed and analyzed through combined experimental and numerical studies.

The response of solidification microstructures to time-dependent growth conditions has been extensively investigated in the context of transient solidification, where the system responds to perturbations applied during growth.[21-29] Such perturbations can lead to delayed adaptations of dendritic spacing and morphology. Kar et al.[30] showed that, during pressure-mediated dendritic growth of succinonitrile, pressure variations significantly affect both growth behavior and dendrite tip radius. More generally, phase-field and experimental studies have demonstrated that spacing evolution under transient conditions proceeds through localized instabilities and exhibits a non-instantaneous response to changes in growth parameters.[31-34]

In contrast, the effect of externally imposed, time-periodic forcing of the pulling velocity on dendritic microstructures has received limited attention. Jackson et al.[35] were among the first to perform directional solidification experiments under periodically varying solidification conditions. They showed that fluctuations in the imposed growth velocity in succinonitrile and carbon tetrabromide samples can lead to the formation of isolated solid crystals through the remelting of dendrite arms. Liu et al.[36] carried out experiments with a continuous decrease in growth velocity to assess the influence of both the magnitude and rate of velocity changes on dendritic length scales. They found that the tip radius and initial arm spacing respond rapidly to variations in growth velocity, whereas the primary spacing evolves more slowly, resulting in significant hysteresis during transient adjustments. Similarly, Ma[37] investigated competitive growth in a dendritic array of succinonitrile-acetone alloy under cyclic variations of the thermal gradient. The results showed that, during increasing and decreasing thermal gradients within the same range, the spacing follows different evolutionary paths, leading to an open hysteresis loop in the primary spacing-thermal gradient relationship.

In particular, the interplay between the forcing timescale and the intrinsic relaxation dynamics of the interface, as well as the resulting morphological instabilities, remains largely unexplored, especially in bulk, three-dimensional growth under purely diffusive conditions. In the present work, the response of dendritic microstructures to oscillating step-like variations of the pulling velocity under microgravity conditions is investigated. Using *in situ* observations from the DECLIC-DSI facility combined with

quantitative phase-field simulations, the resulting forced oscillations of dendrite tip position and radius are analyzed and the conditions leading to tip destabilization are identified. Previous phase-field simulations[38] and thin-sample experiments[39] have shown that tip oscillations can generate sidebranching without noise or periodic forcing through a stable limit cycle that only exists for large enough temperature gradient. There is no experimental evidence for such a limit cycle in the present experiments that use a moderate temperature gradient; sidebranching is noise-driven in the absence of external forcing and periodic forcing can influence both sidebranching and the larger scale dendritic array structure depending on the period of forcing.

The paper is organized as follows. First, the experimental apparatus and procedure are briefly described. Then, the evolution of the microstructure under constant pulling velocity is analyzed, from transient growth to steady state, including primary spacing, dendrite drift, and tip dynamics characterized through side-view observations. Next, step-like pulling velocity experiments are presented, highlighting a period-dependent transition from rapid tip response to delayed morphological dynamics and instability at long periods. Finally, the experimental results are compared with phase-field simulations, demonstrating quantitative agreement and elucidating the mechanisms governing the period-dependent dendritic response.

Experimental procedure and numerical simulations

The DECLIC-DSI setup includes a Bridgman furnace and an experimental cartridge.[40] The cartridge comprises a quartz crucible and a volume compensation system, which is required to accommodate specimen volume variations associated with phase changes. The cylindrical crucible has an inner diameter of 10 mm and a length allowing approximately 10 cm of solidification, enabling the study of the full development of extended patterns, from their initial stages to the steady growth regime.

Figure 1 presents a schematic of the optical apparatus, in which the experimental cartridge is represented as a cylinder with the liquid phase at the top and the solid phase at the bottom. *In situ*

continuous observation generated a large number of images, and bespoke systematic image analysis procedures were developed.[40] The main axial observation mode (Figure 1a) takes advantage of the complete transparency of the experimental cartridge: light emitted by LEDs passes through the cartridge from bottom to top, crossing the interface, whose image is formed on a CCD camera. An example of dendritic pattern is shown in the inset of Figure 1a. Top-view images of the interface are used to study array dynamics and characteristics such as the primary spacing, i.e., the center-to-center distance between nearest-neighbor cells. Along the same optical axis, a Mach-Zehnder interferometer using a He-Ne laser produces interferometric images (example shown in the inset of Figure 1b), which are used for three-dimensional reconstruction of microstructures.[9,41] In addition, the transverse observation mode provides side-view images of the interface (example shown in the inset of Figure 1c), allowing real time characterization of interface motion and macroscopic shape.

The investigated transparent organic compound was a succinonitrile (SCN) - 0.46 wt% camphor alloy prepared using SCN purified by NASA through successive distillation and zone melting. All steps of sample preparation were performed under vacuum to prevent moisture contamination. A single crystalline solid seed with direction <100> parallel to the axial direction is kept unmelted during all experiments. Solidification is carried out by pulling the experimental cartridge from the hot zone toward the cold zone. A thermal gradient G of 12.5 K/cm is imposed by regulated hot and cold zones located above and below the adiabatic region, where the interface was positioned. Further details of the experimental procedure can be found in previous publications.[11,40,42] In standard experiments, samples are typically pulled at a constant velocity V, or velocity jumps are imposed during pulling. In the present work, a constant velocity V = 1.5 μm/s was used but a square wave velocity profile was also applied. In that case, the sample was first pulled at a constant velocity of 1.5 μm/s until the solid-liquid interface reached steady-state conditions, before imposing an oscillating pulling velocity with an amplitude of 1.5 μm/s, resulting in alternating velocities of 0 and 3 μm/s. The oscillation period T ranged from 100 to 2000 s, leading to the variations in the interface temperature of 0.05 K to 1.0 K, respectively.

Phase-field (PF) modeling is a powerful computational approach for solving challenging free-boundary problems and simulating the dynamics of complex interfaces.[43-46] The quantitative PF model used here has been developed over the past decades to quantitatively explore a variety of microstructure dynamics during alloy solidification. This model exploits a thin-interface asymptotic analysis[47,48] and an anti-trapping current[49,50] to accurately describe the solid-liquid interface dynamics while using a computationally tractable diffuse interface width much larger than that of the actual physical interface. Using the latest three-dimensional implementation of this model, parallelized on Graphics Processing Units,[16,20,51] a time-dependent "Thermal Field Calculation" (TFC) is considered,[12] which is completely free of fitting parameters. This approach couples the evolution equations of the phase field and solute field to a full time-dependent calculation of axial (1D) thermal diffusion in the adiabatic zone. The calculation assumes that the temperature field is radially uniform and includes latent heat release at the moving solid-liquid interface. Here, the same PF formulation coupled with the TFC as in Song *et al.*[12] was used, including the stochastic noise implemented in the phase field. The PF simulations use material and simulation parameters for an SCN-0.46 wt% camphor alloy, identical to those employed in recent studies.[10,14,20,52] The simulated solidification conditions are V = 1.5 μm/s and G = 12.5 K/cm. In addition, we consider a regular face-centered cubic (FCC) array structure[15] with a primary spacing of 406.75 μm, which lies within the stable range.[10]

For step-like oscillations of the pulling velocity, the PF simulations follow the experimental protocol: starting from a steady-state dendritic array at the baseline V = 1.5 μm/s, a square-wave forcing of amplitude V_{amp} = 1.5 μm/s is superimposed so that the pulling velocity alternates between 0 and 3 μm/s with a period *T*, which is scanned over a range from 100 to 2000 s.

Results

The microstructure formation was investigated from the initially stationary interface to the steady state for the two pulling conditions considered: the constant velocity, or the oscillating velocity.

1. Constant pulling velocity solidification experiment

In this experiment, a length of 60 mm was solidified at a constant pulling velocity of 1.5 μm/s (refer to online supplementary material videos SM1, for the top-view images, and SM2, for the side-view images). The early stages of solidification exhibit rapid dynamics, characterized by the transient development of the microstructure, followed by a steady state growth regime with stable primary spacing, although the pattern continues to evolve in terms of topological ordering. Selected top-views of the solid-liquid interface at different times are shown in Figure 2 (top images). The corresponding side-views (bottom images) illustrate the recoil of the interface within the furnace as described in previous studies.[11,14] The evolution of the front recoil is shown in Figure 3 (open red circles, right y-axis), where it can be seen that the interface position remains stable from approximately 10 mm of solidification until the end of the experiment.

The process begins at rest ($V = 0$, $t = 0$), with a smooth and convex interface (Figure 2a). After the onset of pulling, a complex array of more or less linear ridges develops along sub-boundaries, followed by the emergence of a relatively uniform corrugation within the sub-grains (Figure 2b). The interface dynamics are initially very rapid, and interface modulations amplify, eventually leading to a well-developed but highly disordered dendritic pattern (Figure 2c). The dynamics then slow down, and a stage of continuous pattern evolution begins (Figure 2d). At this pulling velocity, the interface remains macroscopically convex from the initial stage to steady state.

The pattern is characterized in terms of primary spacing. In each image, individual structures are first identified and labeled, after which a Voronoi tessellation is applied to determine nearest neighbors. The primary spacing is defined as the center-to-center distance between a given structure and its nearest neighbors. Its evolution is shown in Figure 3 (filled black squares, left y-axis), where it continues to

evolve throughout the solidification process. For convex interfaces, as in the present case at 1.5 μm/s, a continuous stretching of the dendritic array occurs as dendrites drift within the interface plane, leading to a steady increase in the primary spacing at a stable interface position.[53] A detailed description of this behavior is given in a previous work.[14]

Figure 4a shows the solid-liquid interface after 48 mm of solidification, with a top-view and the corresponding side-view, including a zoom in the central region of the interface. Owing to the macroscopically convex interface and the relatively large dendrites, the dendrite tips and secondary branches can be clearly distinguished in the side-view observations. The average tip radius value of 38.9 ± 6.4 μm measured from the side-view images on around 10 dendrites, is consistent with measurements previously obtained from direct and interferometric axial images.[9] This experiment was then repeated to verify the feasibility of using the optical zoom available in side-view diagnostic, combined with a high acquisition rate, to characterize the tips (see supplementary video files SM3, for the top-view images, and SM4, for the side-view images). Figure 4b shows side-view images acquired during one of the zoomed acquisition periods: the depth of field is reduced but the tips are very clearly drawn. The average tip radius measured in this experiment, 39.5 ± 7.1 μm, agrees well with the previous measurement and the natural period of sidebranching was estimated to be 94 s. For the applied pulling rate, this value is consistent, in terms of order of magnitude, with the measurements of Pocheau et al.[54] for impure succinonitrile directional solidification.

These experiments demonstrate that dendrite tip measurements can be performed using side-view observations in our device. Combined with step-like variations in the pulling velocity, this approach could enable detailed investigation of sidebranching dynamics.

2. Step-like pulling velocity solidification experiment

These experiments were initiated in the same manner as those described in the previous section, with a pulling velocity of 1.5 μm/s and a thermal gradient of 12.5 K/cm. Once a steady state was reached,

corresponding to an average primary spacing of approximately 450 μm after about 15 mm of solidification, the pulling velocity was made to oscillate between motor stop (0 μm/s) and twice the initial velocity (3 μm/s), with a given period T and for a given duration. After this sequence, the pulling velocity was reset to the initial value (1.5 μm/s) in order to re-establish steady-state conditions, after which the process was repeated with another oscillation period. In the following, the tip position is measured in the laboratory (furnace) reference frame and is defined as the displacement of the solid-liquid interface relative to its steady-state position immediately before the oscillatory forcing sequence. The sign convention follows the image coordinate system used for data analysis (positive downward), so that interface motion toward the hot zone corresponds to negative tip positions, whereas motion toward the cold zone corresponds to positive tip positions.

The first period tested was T = 100 s, which is close to the natural frequency of sidebranching, in order to evaluate its effect on the dynamics (see supplementary video files SM5, for the side-view images, and SM6, for the top-view images). As shown by the curve represented by the blue squares in Figure 5a, the tip position immediately began to oscillate with the imposed period, with an amplitude of approximately 40 μm, a behavior that was not observed prior to the application of the step-like pulling velocity. Using the nominal thermal gradient (12.5 K/cm), the measured tip position amplitude corresponds to an equivalent temperature amplitude of approximately 0.05 K. this conversion is intended only as an order-of-magnitude estimate of the thermal excursion associated with the measured interface displacement. The temperature amplitude predicted by the phase-field simulations remains slightly smaller, partly because the simulations rely on a time-dependent thermal field calculation, in which the local thermal gradient at the interface is smaller than the nominal value and the thermal field partially follows the sample motion. This behavior is more clearly illustrated in the zoom over a two-period interval after the transient recoil phase. During the first oscillation cycles, the tip position progressively recoils within the thermal field, resulting in a final position different from the initial one. In contrast, no clear oscillatory behavior was detected in the tip radius (green open circles), which remains between 30 and 40 μm, comparable to the value prior to forcing (34.2 ± 3.8 μm). The sidebranching emission period

was measured as 120 ± 9 s during the oscillatory regime, slightly higher than before forcing (103 ± 14 s), and decreased again to 116 ± 7 s after the oscillations were stopped. Thus, although no clear oscillatory behavior is observed in either the sidebranching frequency or the overall pattern organization, the imposed oscillation leads to a slight increase in the sidebranching period.

When a period five times larger was applied T = 500 s (see supplementary video files SM7, for the side-view images, and SM8, for the top-view images), the tip position again oscillated with the imposed period (Figure 5b), but with a larger amplitude of about 200 μm (≈ 0.25 K). This scaling is consistent with the increase in period, resulting in an approximately fivefold increase in oscillation amplitude. The tip position exhibits a nearly triangular periodic oscillation, synchronized with the velocity oscillation: it increases when the motor is stopped and decreases at high pulling velocity. The increase and decrease phases occur at the same rate (1.71 ± 0.01 μm/s). Interestingly, for T = 500 s, the tip radius also begins to oscillate with a rather triangular shape but its synchronization with pulling velocity oscillation is not as clear as for the tip position. The tip radius oscillation amplitude is 9.2 μm around a mean value of 36.5 ± 9.3 μm. The sidebranching emission period remains essentially unchanged, with a value of 111 ± 19 s, consistent with the values measured before and after forcing (116 ± 7 s and 117 ± 11 s, respectively). Likewise, no significant modification of the pattern or of the primary spacing is observed, which remains nearly constant (448 ± 37 μm before and 444 ± 52 μm during the oscillatory regime). A similar behavior is found for T = 100 s, where the primary spacing is 445 ± 51 μm before and 447 ± 40 μm during the oscillatory regime. These results indicate that, for short periods (lower than 500 s), the tip shape rapidly adjusts to the instantaneous growth conditions, in agreement with previous experimental[36,37] and numerical studies[34], whereas primary spacing is not affected.

Figures 6a and 6b present the results obtained for the longer periods, T = 1000 s and T = 2000 s. In these cases, the tip position oscillation amplitude increases significantly, reaching approximately 500 μm (≈ 0.625 K) and 725 μm (≈ 0.9 K), respectively. The corresponding side-view and top-view observations are available in the Supplementary Material as Videos SM9–SM12. The tip position evolution remains synchronized with pulling velocity oscillation with a quite triangular general shape; however, the tip

position deviates from the linearity during the motor stop phase. When the motor stops, the tip position initially increases rapidly and then progressively slows down as it approaches its highest value: compared to the motor velocity, the tip initially moves faster so that its position increases before slowing down as the tip velocity decreases. During this phase, the dendrite tips begin to flatten immediately just after the motor stop, as evidenced by the increase in the tip radius. When the pulling velocity is restored (V = 3 μm/s), the tip position decreases rapidly and approximately linearly. However, the tip radius continues to increase (tips flatten) during most of this phase (V = 3 μm/s) and only sharpens abruptly shortly before the next motor stop. This behavior is likely related to local variations of the thermal and solutal fields near the tips, leading to transient tip blunting.[34] The top-view images (Figures 6a) show that the dynamics is no longer solely governed by tip growth, as the interface approaches a nearly planar morphology during part of the cycle.

For T = 2000 s, these effects become even more pronounced (see supplementary video files SM11 and SM12, corresponding to the side-view and top-view observations, respectively). The tip radius reaches significantly larger values during the motor stop phase, and the interface becomes unstable once pulling resumes. The top-view images reveal perturbations developing within the flattened tips as the interface approaches a locally planar morphology. These perturbations subsequently evolve into multiple structures through a coarsening process. Although this may lead to multiple tips originating from a single one, the mechanism differs from classical tip-splitting.[55,56] Most of these structures are unstable and eventually disappear, limiting the extent of the pattern reorganization. The onset of destabilization can also be identified in the tip position signal as a short transient recoil, as highlighted in the zoomed view spanning two oscillation periods. This process temporarily disrupts the local ordering of the dendritic array before it progressively reorganizes during subsequent growth. For both T = 1000 s and T = 2000 s, the final tip position differs slightly from its initial value, whereas the tip radius remains comparable before and after the oscillatory sequence.

The response to step-like variations of the pulling velocity can be interpreted in terms of characteristic relaxation times. Previous studies on pressure-mediated growth of succinonitrile[30] showed

that the tip velocity responds rapidly, whereas the tip radius evolves with a delay due to the adjustment of the thermal field, not only ahead of the tip but also laterally; however, the relaxation times of both quantities remain of the same order. In the present case, the behavior is more complex. While the tip position responds immediately to changes in pulling velocity, following progressive evolutions that can be described by comparable relaxation times, the evolution of the tip radius depends strongly on whether the pulling velocity is increasing or decreasing. Tip flattening begins immediately when the motor stops and continues well beyond this phase. On the other hand, tip sharpening is significantly delayed after the motor restarts, proceeding rapidly once initiated. The immediate response of the tip position, largely independent of the oscillation period, is illustrated in Figure 7a, where the temporal evolution collapses onto similar phase-aligned trajectories. In contrast, the tip radius exhibits a markedly asymmetric response (Figure 7b), characterized by a gradual increase during the low-velocity phase and a delayed but rapid decrease when the pulling velocity is restored. This asymmetry becomes more pronounced as the oscillation period increases.

In the next section, these experimental results are compared with PF simulations to further elucidate the mechanisms governing this dynamical response.

3. Comparison to phase-field simulations

Primary spacing selection mechanisms have been extensively investigated both analytically and experimentally, primarily in thin sample geometries.[57-61] In the context of the present DECLIC-DSI experiments, previous 3D PF simulations performed under the frozen temperature approximation (FTA) were unable to accurately reproduce the experimentally measured primary spacing.[16,20,52] Introducing a more realistic description of the thermal field through the thermal field calculation (TFC) significantly improves the agreement between simulations and experiments.[12] In the frame of the present study, both models have been tested to simulate oscillating pulling velocities. Simulations based on the FTA predict

pronounced sidebranching when the pulling velocity oscillates, whereas the microgravity experiments do not exhibit such strong activity. Simulations with the TFC produce weaker sidebranches than simulations with the FTA. This discrepancy indicates that thermal effects inside the crucible play a role in sidebranching dynamics and must be taken into account. For this reason, all simulations presented here are performed using the TFC framework. In PF simulations with the TFC, stochastic noise also affects the natural sidebranching frequency. As the noise strength is critical for sidebranching kinetics,[38,62] a flat noise of strength 0.01 was introduced, which yields a sidebranching frequency of approximately 100 s. This represents an increase from 77 s in simulations without noise and closely aligns with the experimental measurements of 94 – 97 s. Therefore, noise is included in all simulations presented below.

Figure 8 show the temporal evolution of the tip position (top panels) and tip radius (bottom panels) obtained by PF simulations for oscillation periods T = 500 s (left panels) and T = 900 s (right panels). In both cases, the tip position remains closely synchronized with the imposed pulling velocity, exhibiting an immediate response (i.e., no phase lag) with only minor deviations from the motor dynamics. This is evidenced by the correspondence between points *a*, *b*, *c* and the successive changes in velocity. In contrast, the tip radius exhibits a delayed response relative to the position, as highlighted by the time shifts between corresponding points (*a*–*a′*, *b*–*b′*, *c*–*c′*). For T = 500 s, these delays are nearly identical during both the increasing and decreasing phases of the pulling velocity, indicating a symmetric response of the tip morphology. This behavior is consistent with the experimental observations at the same period, where the tip radius follows the forcing with a limited and nearly constant phase lag. For the longer period (T = 900 s), the response becomes strongly asymmetric. The delay remains small when the pulling velocity decreases, but becomes significantly larger when it increases, as evidenced by the larger separation between *b* and *b′* compared to *a*–*a′* or *c*–*c′*. In addition, the tip radius reaches a minimum value (point *d′*) and remains nearly constant over a finite time interval, with only small variations, before responding to the subsequent change in pulling velocity. This plateau-like behavior reflects a delayed morphological adjustment and is consistent with the experimental observations at T = 1000 s. These

results highlight a transition from a quasi-symmetric and weakly delayed response at short periods to a strongly asymmetric and history-dependent evolution of the tip radius at longer periods, while the tip position remains rapidly slaved to the imposed velocity. For primary spacing 406.75 μm, dendrite tip splitting occurs for $T \geq 2000$ s following the imposed step-like pulling velocity. After the forcing is terminated, the tip velocity and position recover to steady-state values; however, the dendrite morphology does not return to its initial configuration, indicating an irreversible reorganization of the pattern. In experiments, splitting was observed during the forced oscillation, even if it does not lead to stable microstructures and does not affect the pattern organization. To reproduce such behavior in PF simulations, even higher periods must be imposed ($T = 2200$ s).

Figures 9a and 9b compare the oscillation amplitudes obtained experimentally and by PF simulations for the different periods, for the tip radius and tip position, respectively. Overall, very good agreement is observed, with both experiments and simulations showing an increase in oscillation amplitude with increasing period. Figure 9c presents the evolution of the tip radius as a function of the oscillation period, highlighting the maximum, mean, and minimum values. It exhibits that the tip radius is not centered around the mean value corresponding to $V = 1.5$ μm/s. In particular, the maximum radius increases significantly with an increasing period, reflecting a progressive flattening of the interface that can be associated with a more planar morphology. In contrast, the minimum radius varies only weakly (≈ 20 μm) with the period, which explains the *plateau* observed in Figure 8 between *d'* and *c'*, where the tip radius remains nearly constant at its minimum value. A slight discrepancy is observed in the simulations, where the oscillation amplitude during the first period is slightly higher than in subsequent periods, a trend that is not observed experimentally.

Additional PF studies reveal that the oscillation amplitude of the parameters requires several periods to fully develop. When oscillatory forcing is initiated, the tip velocity reaches a steady oscillatory regime after approximately 2000 s for periods between 500 s and 2000 s. Conversely, when the forcing is terminated after a few complete periods, the system requires about 1000 s to 1800 s to return to steady-

state conditions at $V = 1.5$ µm/s. In general, longer oscillation periods lead to longer transient times, both during the onset and after the removal of the oscillatory forcing.

Overall, these results demonstrate that PF simulations quantitatively capture both the amplitude and dynamics of the dendritic response to step-like forcing, providing a consistent framework to interpret the underlying mechanisms observed experimentally.

Conclusions

The present study investigated the response of dendritic microstructures to step-like variations of the pulling velocity under microgravity conditions using *in situ* observations in the DECLIC-DSI facility, complemented by quantitative phase-field simulations. The use of top and side-view observations enabled direct measurements of dendrite tip dynamics, including tip radius and sidebranching frequency, demonstrating the capability of the experimental setup to access key quantities in bulk samples.

When step-like oscillations of the pulling velocity were imposed, the dendritic response was found to strongly depend on the oscillation period. For short periods ($T \leq 500$ s), the tip position and morphology adjust rapidly to the instantaneous growth conditions, with limited impact on primary spacing and pattern organization. In contrast, for longer periods ($T \geq 1000$ s), a clear decoupling emerges between the rapid response of the tip position and the delayed evolution of the tip radius. This leads to phase-lagged and asymmetric morphological dynamics, characterized by progressive tip flattening during low-velocity phases and delayed but rapid sharpening when growth resumes. For sufficiently long periods ($T \geq 2000$ s), this delayed response results in interface destabilization.

Phase-field simulations incorporating a realistic thermal field calculation and stochastic noise quantitatively reproduce both the amplitude and temporal evolution of the experimental observations. In particular, they capture the transition from symmetric to asymmetric responses, the emergence of plateau-

like behavior in the tip radius, and the onset of tip destabilization at long periods. The simulations further confirm that the characteristic timescales of the system control the transition between stable and unstable regimes.

Overall, this combined experimental and numerical study demonstrates that the dendritic response to time-dependent forcing is governed by the interplay between external forcing timescales and intrinsic relaxation dynamics. These findings provide new insight into the control of microstructure formation under non-steady growth conditions and open perspectives for tailoring solidification microstructures through controlled temporal modulation of processing parameters.

DECLIC-DSI-R experimental data used in this study is available in the NASA Physical Sciences Informatics[63] database.

References

1. B. Billia and R. Trivedi, in *Handbook of Crystal Growth* (Bristol: North-Holland, 1993), vol. 1, pp. 899-1074.
2. R. Trivedi, Y. Shen and S. Liu, *Advances in Materials and Materials Processing* (New Delhi: Tata McGraw-Hill Publ. Ltd., 2001), pp. 42-49.
3. M. E. Glicksman, S. R. Coriell and G. B. Mcfadden, *Annu. Rev. Fluid Mech.* 18, 307 (1986).
4. S. H. Davis, *J. Fluid Mech.* 212, 241 (1990). https://doi.org/10.1017/S002211209000194x
5. G. Muller and A. Ostrogorsky, in *Handbook of Crystal Growth* (Amsterdam: North-Holland, 1994), vol. 2B, pp. 709.
6. M. D. Dupouy, D. Camel and J. J. Favier, *Acta Metall.* 37, 1143 (1989). https://doi.org/10.1016/0001-6160(89)90110-7
7. H. Nguyen-Thi, G. Reinhart and B. Billia, *Comptes Rendus Mécanique* 345, 66 (2017). http://dx.doi.org/10.1016/j.crme.2016.10.007
8. S. Akamatsu, S. Bottin-Rousseau, V. T. Witusiewicz, U. Hecht, M. Plapp, A. Ludwig, J. Mogeritsch, M. Serefoglu, N. Bergeon, F. L. Mota, L. Sturz, G. Zimmermann, S. McFadden and W. Sillekens, *Npj Microgravity* 9, 83 (2023). https://doi.org/10.1038/s41526-023-00326-8
9. M. Medjkoune, T. Lyons, F. L. Mota, J. Tian, K. Ji, L. Littles, A. Karma and N. Bergeon, *Phys. Rev. Mat.* In Press, (2026).
10. M. Medjkoune, T. Lyons, F. L. Mota, J. F. Tian, K. H. Ji, L. Littles, A. Karma and N. Bergeon, *Acta Mater.* 292, (2025). https://doi.org/10.1016/j.actamat.2025.120954
11. F. L. Mota, N. Bergeon, D. Tourret, A. Karma, R. Trivedi and B. Billia, *Acta Mater.* 85, 362 (2015). https://doi.org/10.1016/j.actamat.2014.11.024
12. Y. Song, D. Tourret, F. L. Mota, J. Pereda, B. Billia, N. Bergeon, R. Trivedi and A. Karma, *Acta Mater.* 150, 139 (2018). https://doi.org/10.1016/j.actamat.2018.03.012

13. F. L. Mota, J. Pereda, K. Ji, Y. Song, R. Trivedi, A. Karma and N. Bergeon, *Acta Mater.* 204, 116500 (2021). https://doi.org/10.1016/j.actamat.2020.116500
14. F. L. Mota, K. Ji, L. Strutzenberg Littles, R. Trivedi, A. Karma and N. Bergeon, *Acta Mater.*, 118849 (2023). https://doi.org/10.1016/j.actamat.2023.118849
15. Y. Song, F. L. Mota, D. Tourret, K. Ji, B. Billia, R. Trivedi, N. Bergeon and A. Karma, *Nat. Commun.* 14, 2244 (2023). https://doi.org/10.1038/s41467-023-37458-0
16. N. Bergeon, D. Tourret, L. Chen, J. M. Debierre, R. Guerin, A. Ramirez, B. Billia, A. Karma and R. Trivedi, *Phys. Rev. Lett.* 110, 226102 (2013). https://doi.org/10.1103/Physrevlett.110.226102
17. F. L. Mota, N. Bergeon, A. Karma, R. Trivedi and J. M. Debierre, *Phys. Rev. E* 102, 032804 (2020). https://doi.org/10.1103/PhysRevE.102.032803
18. J. Pereda, F. L. Mota, B. Billia, Y. Song, J. M. Debierre, A. Karma, R. Trivedi and N. Bergeon, in *5th Decennial International Conference on Solidification Processing*. (Old Windsor, 2017).
19. J. Pereda, F. L. Mota, J. M. Debierre, B. Billia, R. Trivedi, A. Karma and N. Bergeon, *Phys. Rev. E* 102, (2020). https://doi.org/10.1103/PhysRevE.102.032804
20. D. Tourret, J.-M. Debierre, Y. Song, F. L. Mota, N. Bergeon, R. Guérin, R. Trivedi, B. Billia and A. Karma, *Phys. Rev. E* 92, 2401 (2015). https://doi.org/10.1103/PhysRevE.92.042401
21. J. J. Xu and D. S. Yu, *J. Cryst. Growth* 226, 378 (2001). https://doi.org/10.1016/S0022-0248(01)01381-1
22. W. Losert, D. A. Stillman, H. Z. Cummins, P. Kopczynski, W. J. Rappel and A. Karma, *Phys. Rev. E* 58, 7492 (1998). https://doi.org/10.1103/PhysRevE.58.7492
23. X. W. Qian and H. Z. Cummins, *Phys. Rev. Lett.* 64, 3038 (1990). https://doi.org/10.1103/PhysRevLett.64.3038
24. L. M. Williams, M. Muschol, X. Qian, W. Losert and H. Z. Cummins, *Phys. Rev. E* 48, 489 (1993). https://doi.org/10.1103/PhysRevE.48.489
25. P. Bouissou, A. Chiffaudel, B. Perrin and P. Tabeling, *Europhys. Lett.* 13, 89 (1990). https://doi.org/10.1209/0295-5075/13/1/015
26. P. Bouissou, B. Perrin and P. Tabeling, *Nonlinear Evolution of Spatio-Temporal Structures in Dissipative Continuous Systems* 225, 475 (1990).
27. T. Börzsönyi, T. Tóth-Katona, A. Buka and L. Gránásy, *Phys. Rev. E* 62, 7817 (2000). https://doi.org/10.1103/PhysRevE.62.7817
28. M. Fell and J. Bilgram, *Phys. Rev. E* 75, (2007). https://doi.org/10.1103/PhysRevE.75.061603
29. P. Peng, X. Z. Li, Y. Q. Su and J. J. Guo, *Mater. Chem. Phys.* 177, 496 (2016). https://doi.org/10.1016/j.matchemphys.2016.04.060
30. P. Kar, J. C. LaCombe and M. B. Koss, *Mater. Sci. Technol.* 20, 1273 (2004). https://doi.org/10.1179/026708304225022223
31. X. Lin, W. Huang, J. Feng, T. Li and Y. Zhou, *Acta Mater.* 47, 3271 (1999). https://doi.org/10.1016/S1359-6454(99)00166-4
32. W. Losert, B. Q. Shi, H. Z. Cummins and J. A. Warren, *Phys. Rev. Lett.* 77, 889 (1996). https://doi.org/10.1103/physrevlett.77.889
33. M. Amoorezaei, S. Gurevich and N. Provatas, *Acta Mater.* 58, 6115 (2010). https://doi.org/10.1016/j.actamat.2010.07.029
34. W. J. Zheng, Z. B. Dong, Y. H. Wei and Y. Wang, *Cryst. Res. Technol.* 49, 777 (2014). https://doi.org/10.1002/crat.201400119
35. K. A. Jackson, J. D. Hunt, D. R. Uhlmann and T. P. Seward, 1967.
36. S. Liu, S. Z. Lu and A. Hellawell, *J. Cryst. Growth* 234, 740 (2002). https://doi.org/10.1016/s0022-0248(01)01680-3
37. D. X. Ma, *J. Cryst. Growth* 260, 580 (2004). https://doi.org/10.1016/j.jcrysgro.2003.08.071
38. B. Echebarria, A. Karma and S. Gurevich, *Phys. Rev. E* 81, 1608 (2010). https://doi.org/10.1103/physreve.81.021608
39. T. Lyons, *Dendrite sidebranches in directional solidification*, Iowa State University (2022).

40. F. L. Mota, M. Medjkoune, L. S. Littles, A. Karma and N. Bergeon, *Rev. Sci. Instrum.* 94, 15 (2023). https://doi.org/10.1063/5.0150391
41. N. Bergeon, C. Weiss, N. Mangelinck-Noel and B. Billia, *Trans. Indian. Inst. Met.* 62, 455 (2009). https://doi.org/10.1007/s12666-009-0061-6
42. N. Bergeon, A. Ramirez, L. Chen, B. Billia, J. H. Gu and R. Trivedi, *J. Mat. Sci.* 46, 6191 (2011). https://doi.org/10.1007/s10853-011-5382-2
43. L. Q. Chen, *Annu. Rev. Mater. Res.* 32, 113 (2002). https://doi.org/10.1146/annurev.matsci.32.112001.132041
44. W. J. Boettinger, J. A. Warren, C. Beckermann and A. Karma, *Annu. Rev. Mater. Res.* 32, 163 (2002). https://doi.org/10.1146/annurev.matsci.32.101901.155803
45. J. J. Hoyt, M. Asta and A. Karma, *Mater. Sci. Eng., R* 41, 121 (2003). https://doi.org/10.1016/s0927-796x(03)00036-6
46. I. Steinbach, *JOM* 65, 1096 (2013). https://doi.org/10.1007/s11837-013-0681-5
47. A. Karma and W. J. Rappel, *Phys. Rev. E* 53, 3017 (1996). https://doi.org/10.1103/physreve.53.r3017
48. A. Karma and W. J. Rappel, *Phys. Rev. E* 57, 4323 (1998). https://doi.org/10.1103/physreve.57.4323
49. A. Karma, *Phys. Rev. Lett.* 87, 115701 (2001). https://doi.org/10.1103/physrevlett.87.115701
50. B. Echebarria, R. Folch, A. Karma and M. Plapp, *Phys. Rev. E* 70, 1604 (2004). https://doi.org/10.1103/physreve.70.061604
51. A. J. Clarke, D. Tourret, Y. Song, S. D. Imhoff, P. J. Gibbs, J. W. Gibbs, K. Fezzaa and A. Karma, *Acta Mater.* 129, 203 (2017). http://dx.doi.org/10.1016/j.actamat.2017.02.047
52. J. Pereda, F. L. Mota, L. Chen, B. Billia, D. Tourret, Y. Song, J. M. Debierre, R. Guérin, A. Karma, R. Trivedi and N. Bergeon, *Phys. Rev. E* 95, 2803 (2017). https://doi.org/10.1103/PhysRevE.95.012803
53. S. Bottin-Rousseau and A. Pocheau, *Phys. Rev. Lett.* 87, 6101 (2001). https://doi.org/10.1103/Physrevlett.87.076101
54. A. Pocheau, S. Bodea and M. Georgelin, *Phys. Rev. E* 80, (2009). https://doi.org/10.1103/PhysRevE.80.031601
55. H. Honjo, S. Ohta and Y. Sawada, *Phys. Rev. Lett.* 55, 841 (1985). https://doi.org/10.1103/PhysRevLett.55.841
56. B. Utter, R. Ragnarsson and E. Bodenschatz, *Phys. Rev. Lett.* 86, 4604 (2001). https://doi.org/10.1103/PhysRevLett.86.4604
57. R. N. Grugel and Y. Zhou, *Met. Trans. A* 20, 969 (1989). https://doi.org/10.1007/Bf02651662
58. K. Somboonsuk, J. T. Mason and R. Trivedi, *Met. Trans. A* 15, 967 (1984). https://doi.org/10.1007/Bf02644688
59. R. Trivedi and K. Somboonsuk, *Mat. Sci. Eng.* 65, 65 (1984). https://doi.org/10.1016/0025-5416(84)90200-3
60. K. Somboonsuk and R. Trivedi, *Acta Metall.* 33, 1051 (1985). https://doi.org/10.1016/0001-6160(85)90198-1
61. R. Trivedi and K. Somboonsuk, *Acta Metall.* 33, 1061 (1985). https://doi.org/10.1016/0001-6160(85)90199-3
62. A. Karma and W. J. Rappel, *Phys. Rev. E* 60, 3614 (1999). https://doi.org/10.1103/PhysRevE.60.3614
63. Author, *DEvice for the study of Critical LIquids and Crystallization Directional Solidification Insert-Reflight(DECLIC DSI-R)*, https://doi.org/10.60555/wc3d-md27 (2023).

Acknowledgments

The authors acknowledge financial support from the *Centre national d'études spatiales* (CNES), France (ROR: https://ror.org/04h1h0y33), within the framework of the DECLIC space mission. This work is based on observations performed with the DECLIC-DSI (*Directional Solidification Insert* of the *DEvice for the study of Critical LIquids and Crystallization*) facility aboard the International Space Station (ISS). This work was also supported by *National Aeronautics and Space Administration* (NASA) under Grant No. 80NSSC22K0664. K.J. and Y.S. acknowledge partial support from *Lawrence Livermore National Laboratory* under Contract DE-AC52–07NA27344.

Conflicts Of Interest

The authors declare that they have no known competing financial interests or personal relationships that could have appeared to influence the work reported in this paper.

Figures

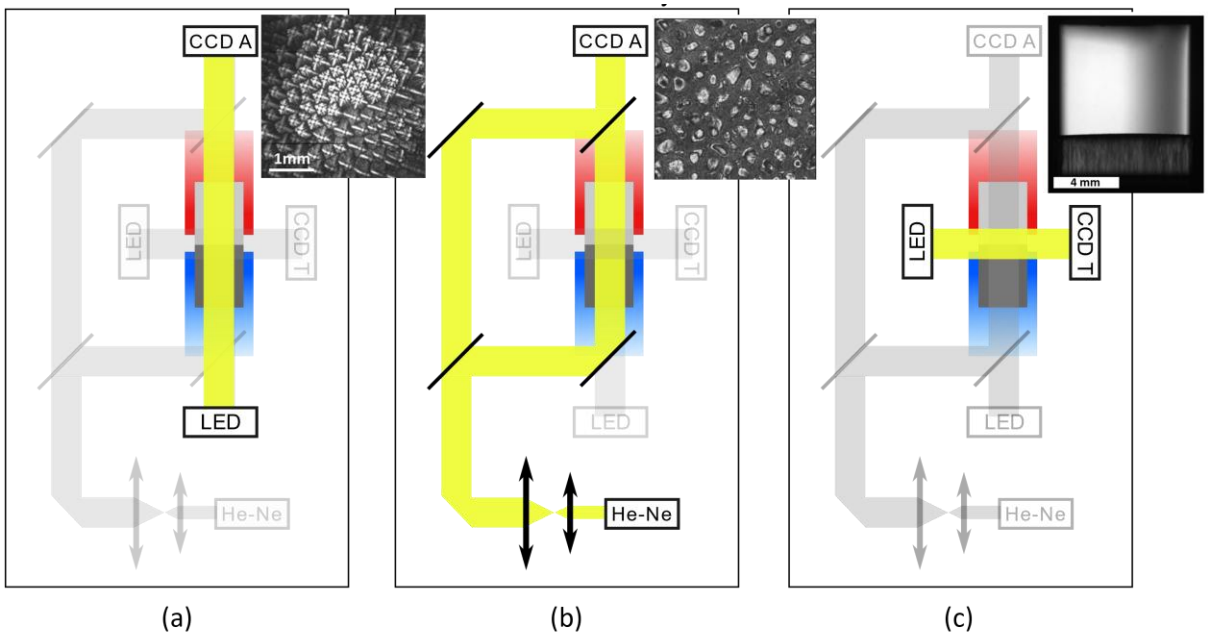

Figure 1 – Schematic representation of the optical acquisition system in DECLIC-DSI and examples of raw images (top insets): (a) axial direct; (b) axial interferometric; and (c) transverse direct. The red and blue rectangles represent the hot and cold zones of the Bridgman furnace, respectively. The labels A and T denote the axial and transverse views of the sample. The yellow regions indicate the light path—white in (a) and (c), and a laser beam in (b).

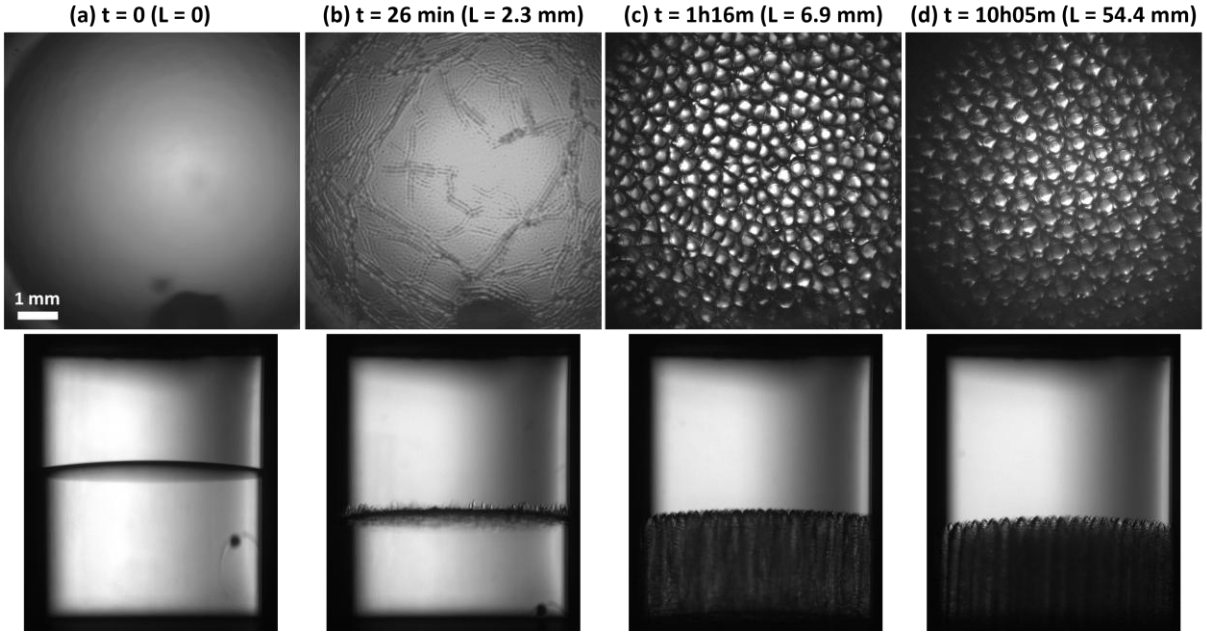

Figure 2 – Sequence of interfacial microstructure formation in SCN–0.46 wt% camphor at a pulling velocity of V = 1.5 μm/s. Top images show top-views of the solid-liquid interface, whereas bottom images show side-views. t denotes the elapsed solidification time and L the corresponding solidification length ($L = Vt$). Videos SM1 and SM2 in the Supplementary Material correspond to the top-view and side-view observations, respectively.

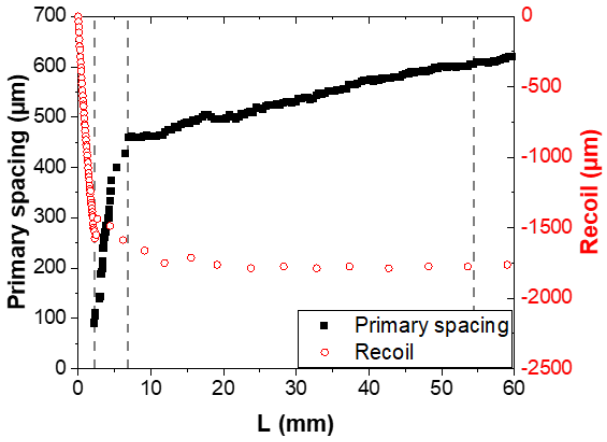

Figure 3 – Evolution of the primary spacing (filled black squares, left y-axis) and front recoil (open red circles, right y-axis) as a function of the solidified length ($L=Vt$) at $V = 1.5$ µm/s. The vertical dashed lines indicate the times corresponding to the images in Figure 2.

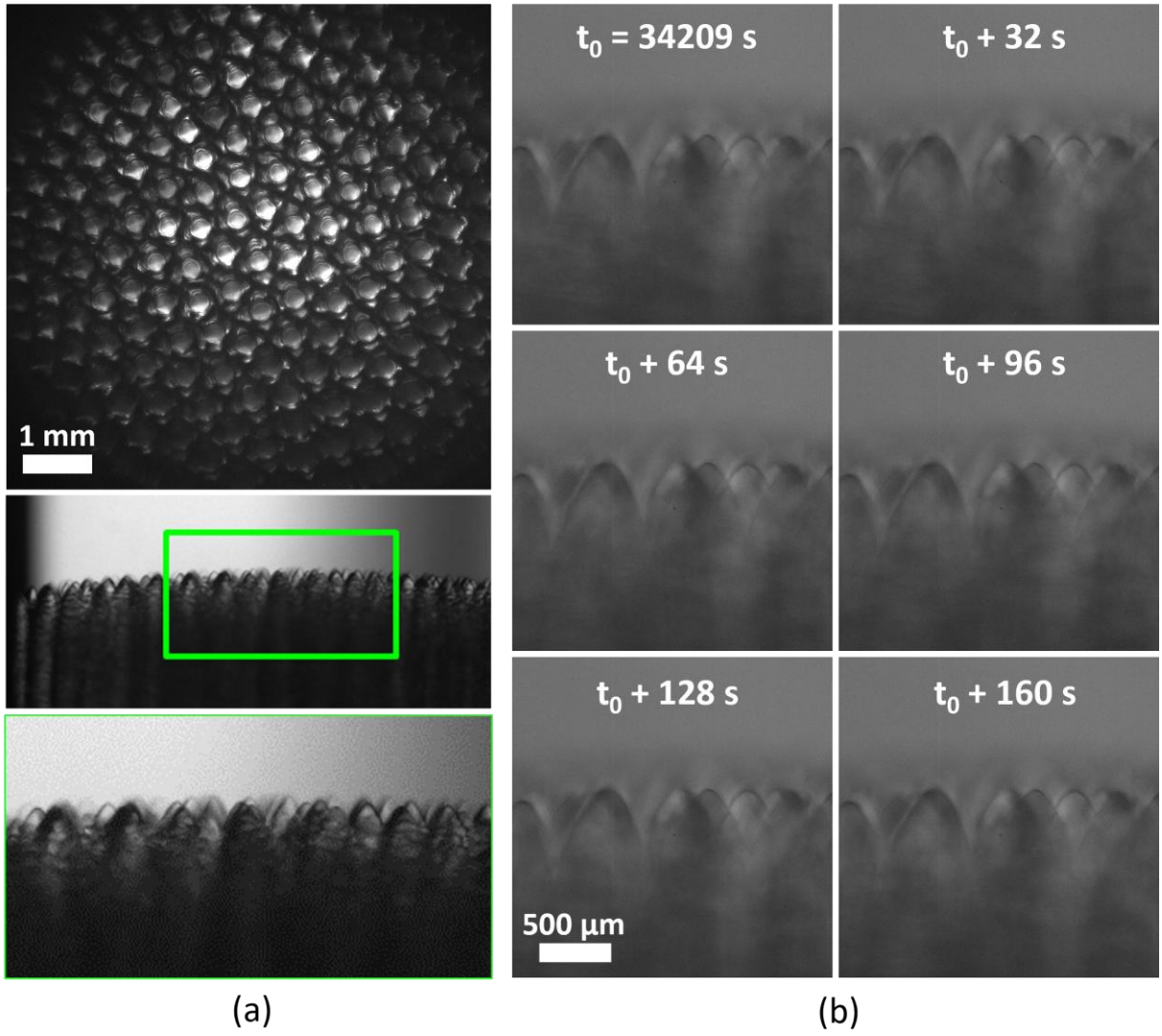

Figure 4 – Images of the solid–liquid interface of an SCN-0.46 wt% camphor alloy for V = 1.5 µm/s and G = 12.5 K/cm under microgravity: (a) top-view with the corresponding side-view (including a zoomed region); (b) *in situ* time sequence of zoomed side-view observations.

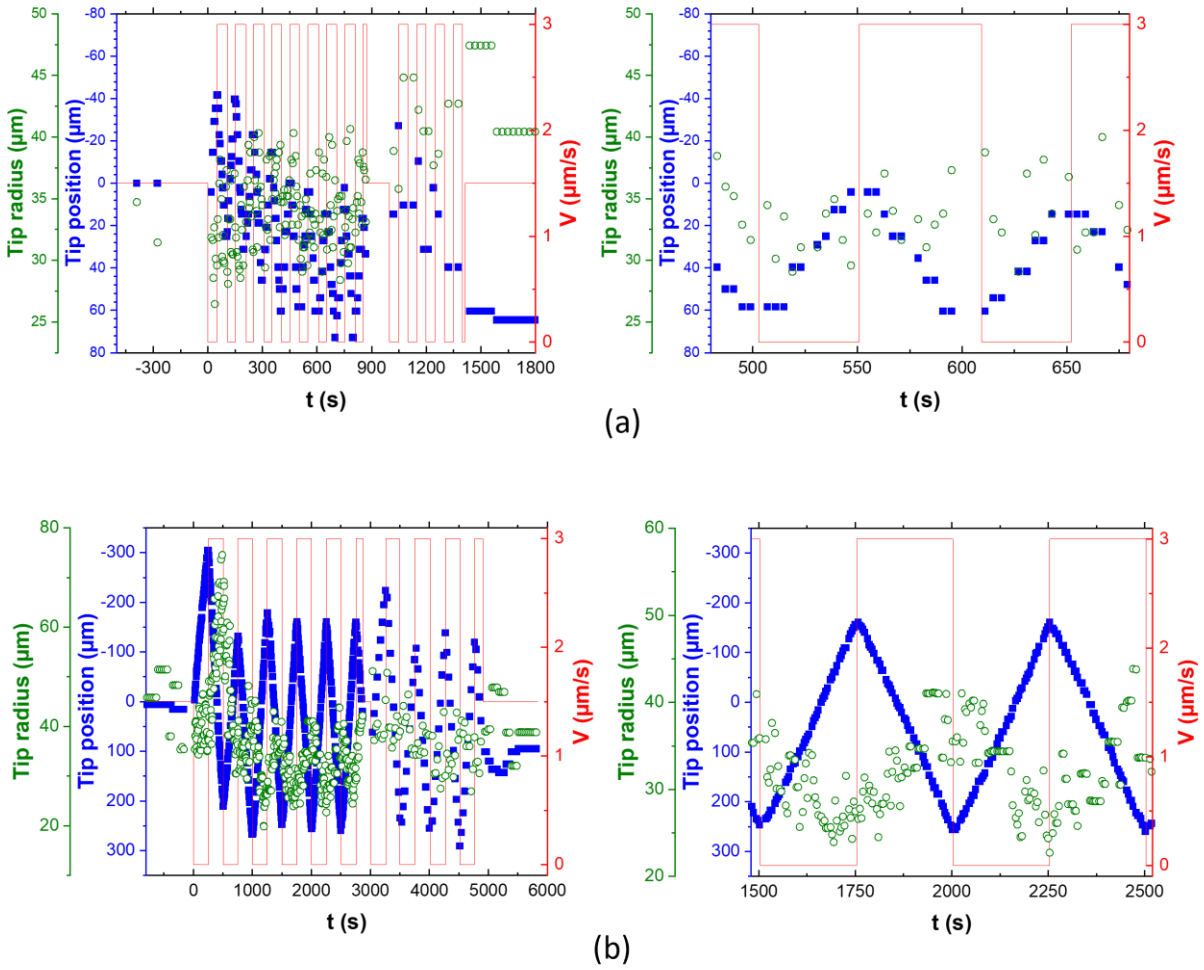

Figure 5 – Temporal evolution of the tip radius (green open circles) and tip position (blue filled squares) during several cycles of step-like pulling velocity (red curve, right y-axis) with an oscillation period of (a) T = 100 s and (b) T = 500 s: whole sequence and zoom on 2 periods. The corresponding side-view and top-view observations are available in the Supplementary Material as Videos SM5–SM8.

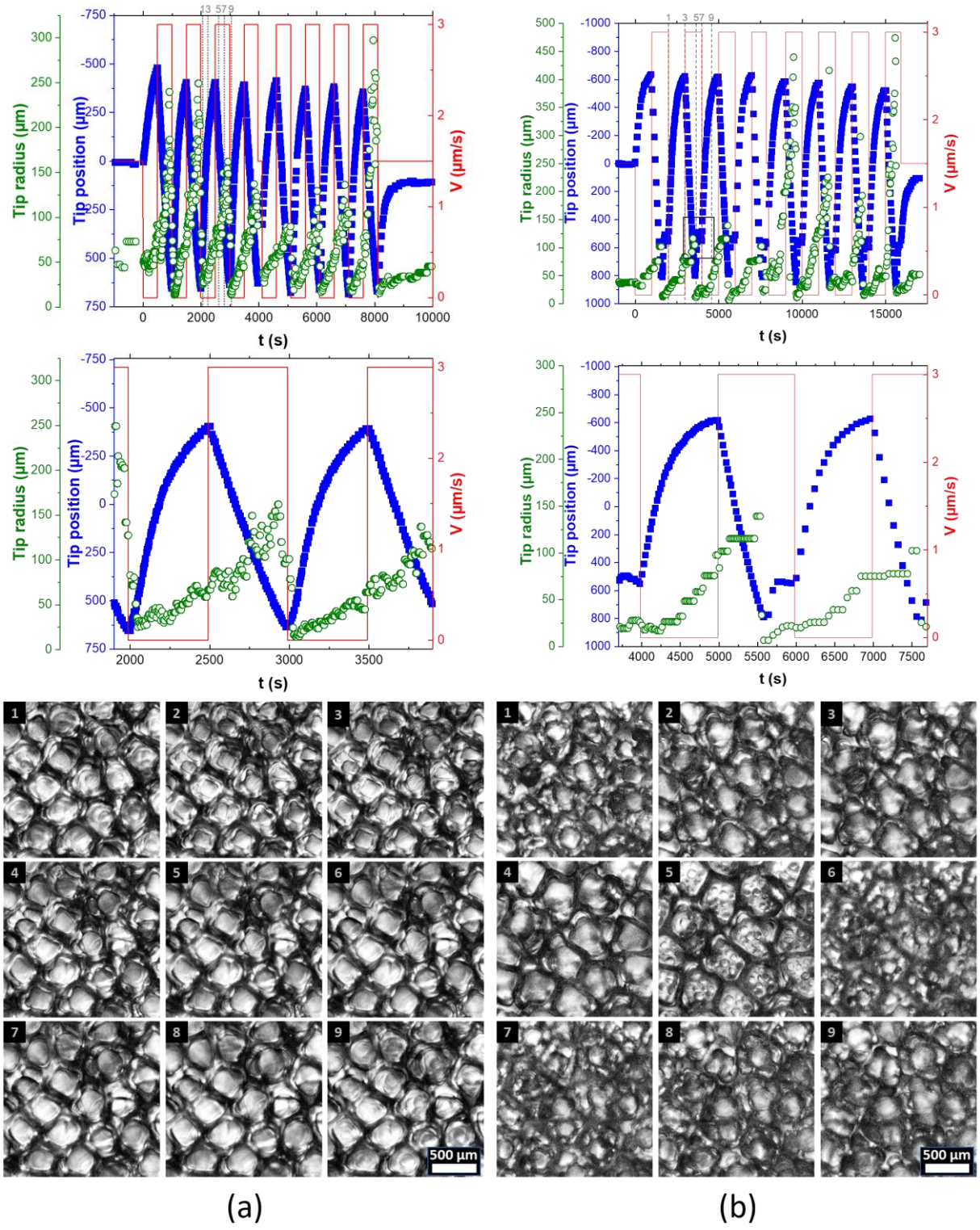

Figure 6 – Temporal evolution of the tip radius (green open circles) and tip position (blue filled squares) during several cycles of step-like pulling velocity (red curve, right y-axis) with an oscillation period of (a) $T = 1000$ s and (b) $T = 2000$ s, including a zoomed region in two periods. Top-

view images between the moments 1 and 9 indicated by the vertical dashed lines in the plot. The corresponding side-view and top-view observations are available in the Supplementary Material as Videos SM9–SM12.

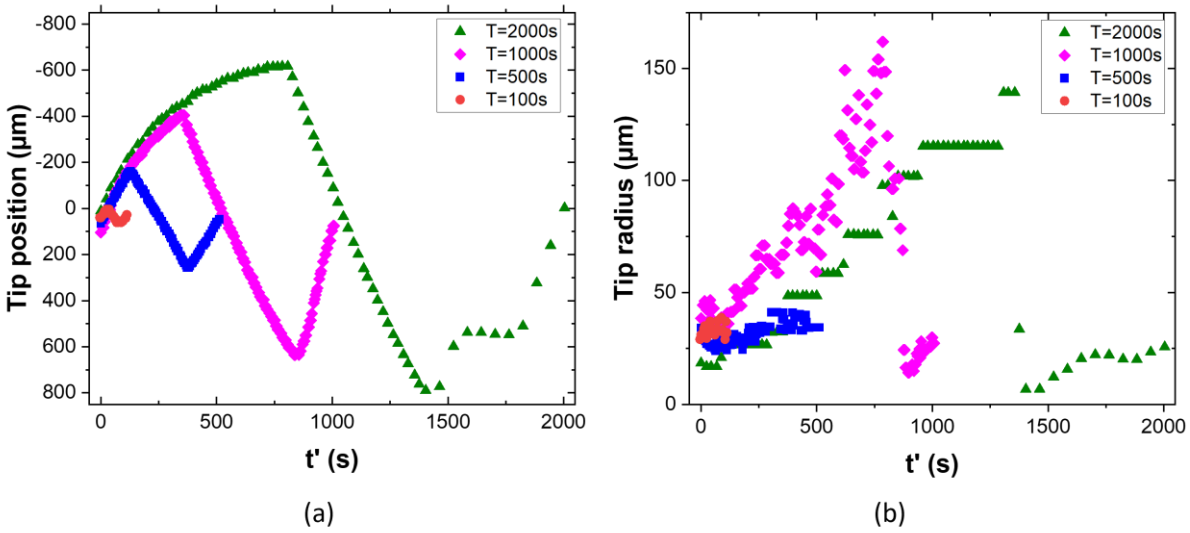

Figure 7 – One period evolution of (a) tip position and (b) tip radius for different oscillation periods T = 100, 500, 1000, and 2000 s. Time is scaled to start in a middle of the half-period corresponding to motor stop.

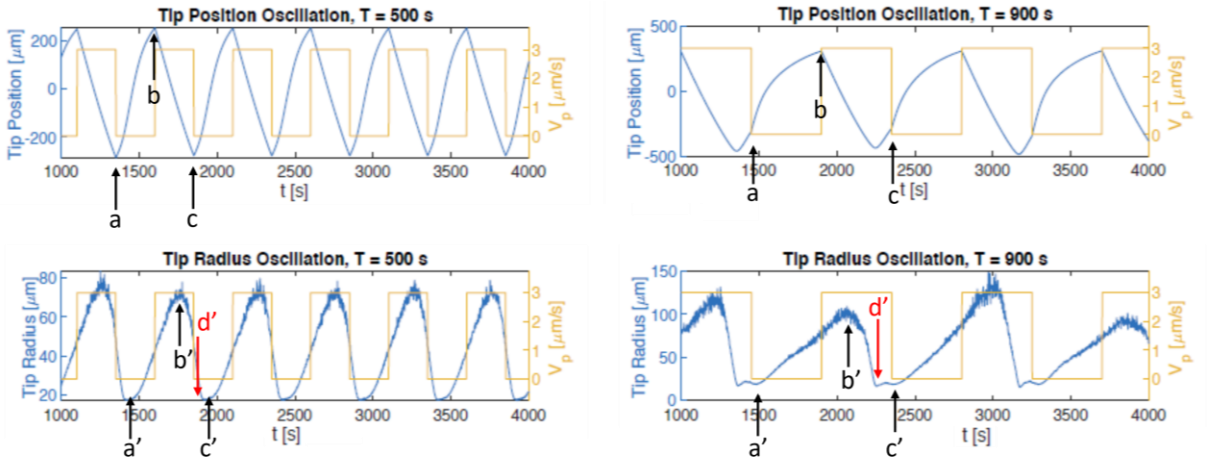

Figure 8 – Temporal evolution of the tip position (top) and tip radius (bottom) obtained by phase-field simulations for oscillation periods T = 500 s (left) and T = 900 s (right), together with the imposed pulling velocity (brown curves, right y-axis). Points *a* and *c* correspond to motor

stop, whereas *b* corresponds to motor restart. Points *a'* and *c'* indicate the onset of the increase in tip radius following motor stop, *b'* the maximum tip radius, and *d'* the minimum tip radius, at which the tip radius remains nearly constant until the next motor stop (point *c*). The time intervals $a - a'$, $b - b'$, and $c - c'$ illustrate the delay between the imposed changes in pulling velocity and the morphological response of the dendrite tip. Phase-field simulations were performed for the directional solidification of an SCN-0.46 wt% camphor alloy, with a temperature gradient G = 12.5 K/cm and an average pulling velocity V = 1.5 μm/s.

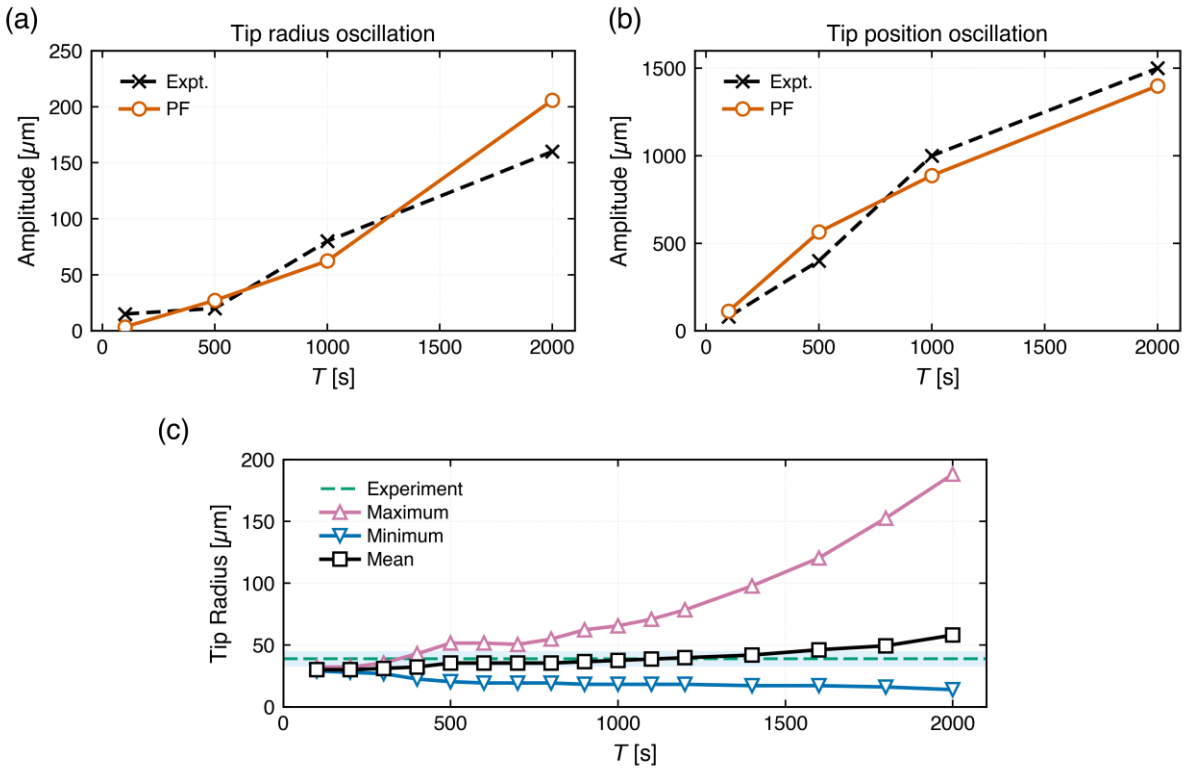

Figure 9 – Comparison between experimental and simulated oscillation amplitudes of (a) tip radius and (b) tip position. (c) Maximum, minimum and mean tip radius as function of the oscillation period. Phase-field simulations were performed for the directional solidification of an SCN-0.46 wt% camphor alloy, with a temperature gradient G = 12.5 K/cm and an average pulling velocity V = 1.5 μm/s.